SPACE SCIENCES

Copyright © 2017 The Authors, some rights reserved; exclusive licensee American Association for the Advancement of Science. No claim to original U.S. Government Works. Distributed under a Creative Commons Attribution NonCommercial License 4.0 (CC BY-NC).

Time-of-day–dependent global distribution of lunar surficial water/hydroxyl

Christian Wöhler,[1]* Arne Grumpe,[1] Alexey A. Berezhnoy,[2] Vladislav V. Shevchenko[2]

A new set of time-of-day–dependent global maps of the lunar near-infrared water/hydroxyl (H_2O/OH) absorption band strength near 2.8 to 3.0 μm constructed on the basis of Moon Mineralogy Mapper (M^3) data is presented. The analyzed absorption band near 2.8 to 3.0 μm indicates the presence of surficial H_2O/OH. To remove the thermal emission component from the M^3 reflectance spectra, a reliable and physically realistic mapping method has been developed. Our maps show that lunar highlands at high latitudes show a stronger H_2O/OH absorption band in the lunar morning and evening than at midday. The amplitude of these time-of-day–dependent variations decreases with decreasing latitude of the highland regions, where below about 30°, absorption strength becomes nearly constant during the lunar day at a similar level as in the high-latitude highlands at midday. The lunar maria exhibit weaker H_2O/OH absorption than the highlands at all, but showing a smaller difference from highlands absorption levels in the morning and evening than at midday. The level around midday is generally higher for low-Ti than for high-Ti mare surfaces, where it reaches near-zero values. Our observations contrast with previous studies that indicate a significant concentration of surficial H_2O/OH at high latitudes only. Furthermore, although our results generally support the commonly accepted mechanism of H_2O/OH formation by adsorption of solar wind protons, they suggest the presence of a more strongly bounded surficial H_2O/OH component in the lunar highlands and parts of the mare regions, which is not removed by processes such as diffusion/thermal evaporation and photolysis in the course of the lunar day.

INTRODUCTION

Near-infrared reflectance spectra acquired by the Moon Mineralogy Mapper (M^3) instrument (*1*) are known to exhibit an absorption band around 2.8- to 3.0-μm wavelength, indicating the presence of surficial water (H_2O) and/or hydroxyl (OH) (*2*). Previous studies have led to the general understanding that a strong H_2O/OH absorption band is only present in the lunar highlands at high selenographic latitudes beyond 50° to 60° north and south, respectively, whereas the absorption band has been found to be weak or absent at lower latitudes (*2*). The dependence of the H_2O/OH absorption band on time of day has not been examined in the study by Pieters *et al.* (*2*). The solar wind has been suggested by Pieters *et al.* (*2*) as the most likely source of the H_2O/OH species that elicit the 3-μm band, but hydrated minerals are also considered possible. A strong contrast in H_2O/OH absorption depth between mare and highland terrains has been described in the study by McCord *et al.* (*3*), with mare surfaces exhibiting a near-zero absorption strength. Furthermore, the results of McCord *et al.* (*3*) suggest a time-of-day–dependent variation of the H_2O/OH absorption strength, which is found to be strongly correlated with the illumination conditions and, thus, the local surface temperature. Near-infrared spectra acquired during the Deep Impact mission exhibit variations of the lunar H_2O/OH absorption depth with selenographic latitude and local time of day (*4*). For a region in Mare Imbrium, the H_2O/OH absorption depth has been found to decrease to a near-zero value, whereas in a highland region south of Mare Humboldtianum, the H_2O/OH absorption depth decreases at midday to about 50% of its morning value (*4*). For the region around the lunar crater Boguslawsky located in the illuminated southern polar nearside highlands, the H_2O/OH absorption strength has been found to decrease from a high level in the lunar morning to a lower but still nonzero level at midday (*5*). For estimation of the same method for surface temperature estimation and thermal emission removal as in this paper has been used in the study by Wöhler *et al.* (*5*). For a few selected points on the lunar surface, Bandfield *et al.* (*6*) found that the H_2O/OH absorption band is present not only at high latitudes but also at low latitudes under both oblique and steep illumination. The data of Bandfield *et al.* (*6*) suggest that the H_2O/OH absorption strength is largely independent of solar incidence angle. Inside the lunar swirl Reiner Gamma, the H_2O/OH absorption band is observed in the study by Bandfield *et al.* (*6*) to be less strong than outside the swirl, which leads to the conclusion of a solar wind origin of the H_2O-related absorption near 2.95 μm (*6*). The time-of-day dependence of the H_2O/OH absorption strength is not examined specifically by Bandfield *et al.* (*6*). For the results obtained from the study by Bandfield *et al.* (*6*), the method of Bandfield *et al.* (*7*) for surface temperature estimation was used, which accounts for the surface roughness.

Data acquired by the Lunar Prospector Neutron Spectrometer indicate the presence of hydrogen near the lunar poles (*8*), interpreted as H_2O ice therein. As an alternative explanation, Starukhina and Shkuratov (*9*) proposed that the Lunar Prospector neutron flux–based observations of polar H, described, for example, in the study by Feldman *et al.* (*8*), may result from solar wind protons, which are adsorbed by the regolith and remain stable because of the low surface temperature in the lunar polar regions. Starukhina and Shkuratov (*9*) suggested that protons from Earth's magnetotail are a source of H in permanently shadowed regions (*9*). Hydrogen maps of higher resolution have been constructed using data of the Lunar Reconnaissance Orbiter (LRO) Lunar Exploration Neutron Detector (LEND), where water-equivalent hydrogen abundances of up to 0.5 weight % (wt %) at depths of up to 1 m have been inferred for permanently shadowed regions at high latitudes (*10*). Furthermore, LEND data indicate an increased hydrogen content in the upper 1-m layer on pole-facing slopes at high selenographic latitudes (*11*), as well as time-of-day–dependent variations of the hydrogen content (*12*). A study by Livengood *et al.* (*12*) found the equatorial hydrogen concentration

[1]Image Analysis Group, Technical University of Dortmund, Otto-Hahn-Str. 4, D-44227 Dortmund, Germany. [2]Sternberg Astronomical Institute, Moscow State University, Universitetskij pr., 13, 119234 Moscow, Russia.
*Corresponding author. Email: christian.woehler@tu-dortmund.de

to be maximal in the early morning, decreasing to its minimum in the late afternoon. Livengood *et al.* (*12*) invoked volatile species originating from larger depth below the lunar surface to explain the observed hydrogen concentrations, which are so high that hydrogen delivery by the solar wind and meteoroid impacts alone is considered insufficient (*12*).

However, a factor impeding analysis of the H_2O/OH absorption band depth is the thermal emission component that severely affects the spectral radiances measured by M^3 in the corresponding wavelength range, which needs to be corrected on the basis of an accurate estimation of the surface temperature. For the M^3 level 2 spectral reflectance data released on the Planetary Data System (PDS) (*13*), the approach of Clark *et al.* (*14*) has been used for surface temperature estimation and thermal emission removal (*15*). Clark *et al.* (*14*) point out that the method proposed therein yields inaccurate surface temperature estimates in the presence of a strong pyroxene-related spectral absorption band around 2 μm. These absorption bands are present throughout the lunar maria, hence in significant fractions of the lunar surface. Furthermore, especially for high incidence angles (oblique illumination), the rough surface of the Moon cannot be regarded as isothermal, that is, being characterized by a single temperature; it is instead characterized by a mixture of different temperature values due to the nonuniform inclination of different surface facets with respect to illumination direction (*7*, *16*). An approach to account for the surface roughness when estimating the surface temperature is proposed in the study by Bandfield *et al.* (*7*), which is based on statistical modeling of the facet inclination. The methods for artificial generation of rough surfaces and estimation of their temperatures under solar illumination introduced by Davidsson *et al.* (*16*) and Bandfield *et al.* (*7*), respectively, will be discussed in some detail in Materials and Methods. A preliminary analysis by Bandfield *et al.*, which probed how accounting for the surface roughness influences the derived strength of the lunar H_2O/OH absorption band (*6*, *17*), relying on the surface temperature estimation method of Bandfield *et al.* (*7*), suggests that the surface temperatures estimated with the method of Clark *et al.* (*14*) are too low and that the H_2O/OH absorption band is actually more pronounced than previously assumed. The results of Wöhler *et al.* (*5*) are in accordance with this general finding. Hence, H_2O/OH absorption band depths derived from the M^3 level 2 radiance data on the PDS should be treated with care.

Thus, this paper concentrates on aspects of (i) the spatial distribution of lunar surficial H_2O/OH on the lunar surface, (ii) the strength of the time-of-day–dependent variations of the density of surficial H_2O/OH, and (iii) the relevance of the mechanism of solar wind proton adsorption as an explanation of the observed behavior of the H_2O/OH absorption band depth.

RESULTS

Overview of the M^3 data processing framework

Here, a new set of time-of-day–dependent global maps of the lunar H_2O/OH absorption strength is presented. Our approach completely relies on the M^3 level 1B radiance data set available on the PDS. The thermal emission removal has been performed on the basis of the method introduced by Wöhler *et al.* (*5*). This method relies on the thermal equilibrium–based approach of Shkuratov *et al.* (*18*) but extends it by incorporating an iterative adjustment of surface temperature and spectral reflectance until both quantities have converged toward a consistent solution. Furthermore, a correction for surface roughness is applied using an approach similar to that of Davidsson *et al.* (*16*). The Hapke model (*19*, *20*) is used to normalize the spectral reflectance to a uniform illumination and viewing geometry. The effect of local topography on the reflectance spectra is eliminated using the GLD100 topographic map (*21*). The spatial resolution of the original M^3 data set of 140 m per pixel (*1*) has been reduced to 20 pixels per degree longitude and latitude, corresponding to about 1.5 km at the lunar equator. The resulting normalized reflectance spectra were then used to compute the relative H_2O/OH band depth integrated over M^3 channels 78 to 84 between 2697 and 2936 nm (here termed OHIBD) after division by a linear continuum fitted to M^3 channels 74 to 77 (2537 to 2657 nm) just shortward of the H_2O/OH absorption band [see the study by Wöhler *et al.* (*5*) and Materials and Methods for details on our data processing framework].

A typical M^3 reflectance spectrum illustrating the removal of the thermal emission component, comparing our method with that of Clark *et al.* (*14*), is shown in Fig. 1. The shape of the mare soil reflectance spectrum corrected with our method (Fig. 1A) is largely linear with weak absorption bands near 1 and 2 μm, whereas the highland soil reflectance spectrum is of convex shape (Fig. 1B). This is a plausible result because similar shapes have been measured in the laboratory for the finely grained fractions of, for example, Apollo mare sample 10084 (*22*) and Apollo highland sample 62231 (*23*), respectively. However, the reflectance spectra shown in the study by Taylor *et al.* (*22*, *23*) do not extend into the wavelength range of the H_2O/OH absorption band.

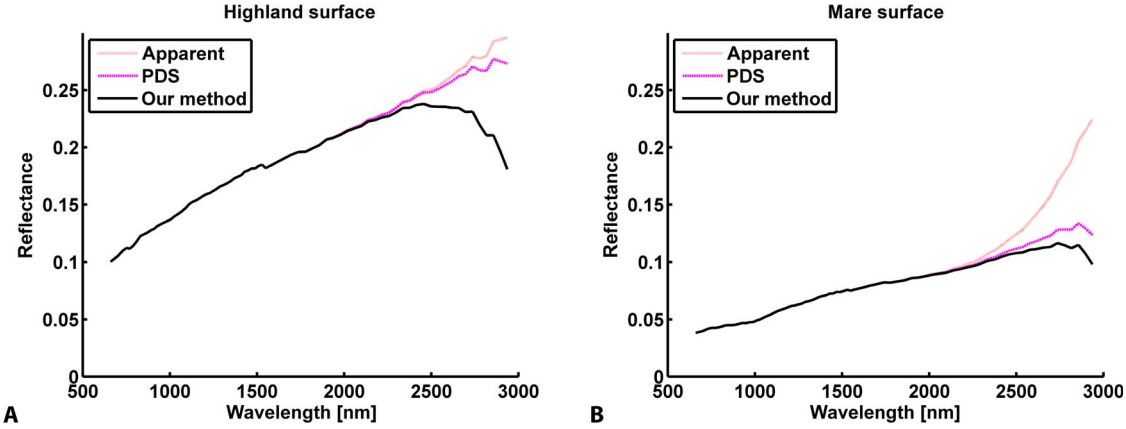

Fig. 1. Typical M^3 reflectance spectra illustrating the removal of the thermal emission component using the surface temperature taken from the PDS and obtained with our method, respectively. (**A**) Mare surface (12.64°E, 20.00°N; local time, 12:45). (**B**) Highland surface (167.90°E, 20.01°N; local time, 11:32).

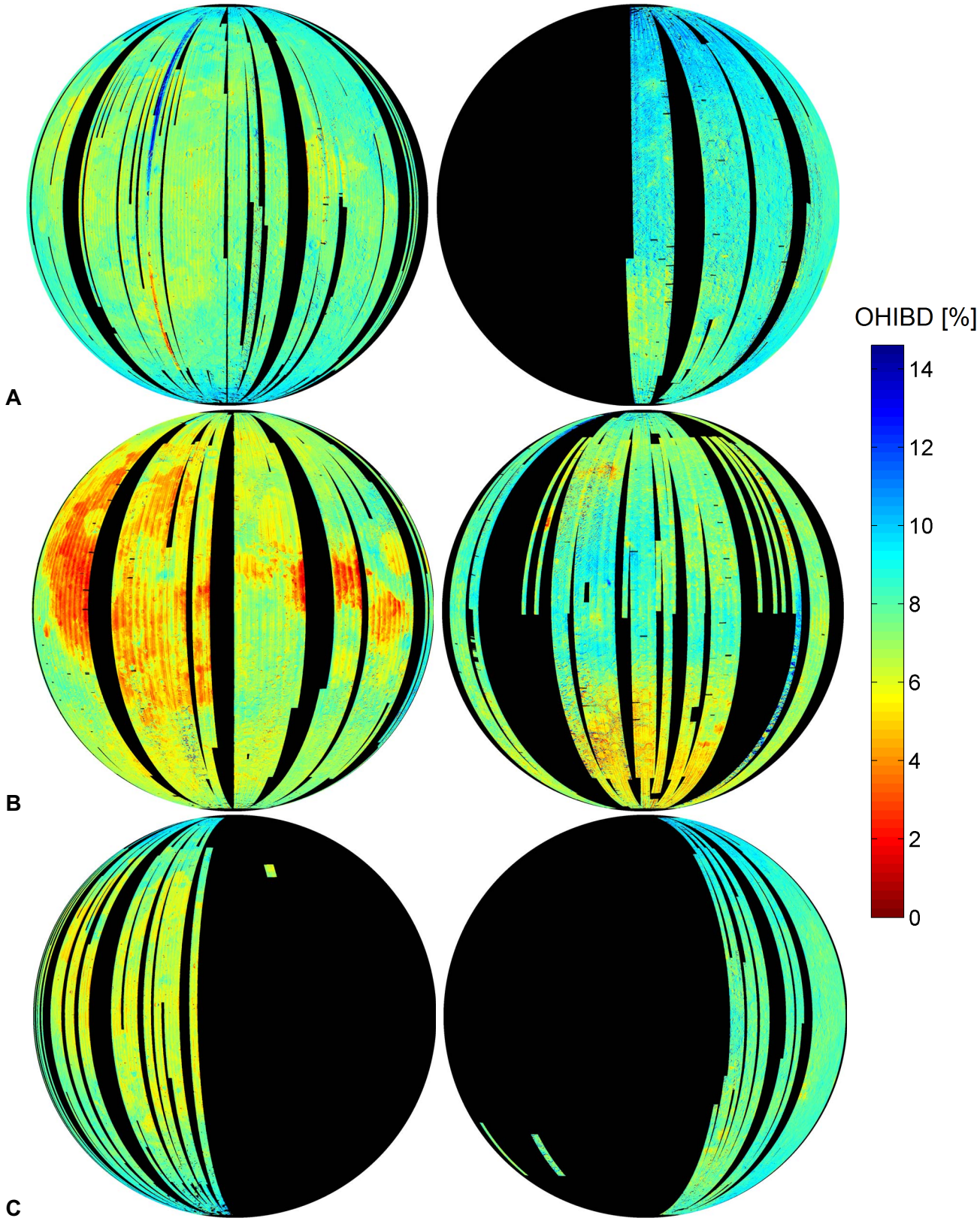

Fig. 2. Global OHIBD maps in orthographic projection (9° RMS slope). The lunar nearside (central meridian 0°) and the farside (central meridian 180°) are shown in the left and right columns, respectively. Black pixels denote missing data. (**A**) Morning OHIBD maps (local time, 07:00 to 08:00). (**B**) Midday OHIBD maps (nearside: local time, 12:00 to 14:00; farside: local time, 10:00 to 12:00). (**C**) Evening OHIBD maps (local time, 16:00 to 17:00).

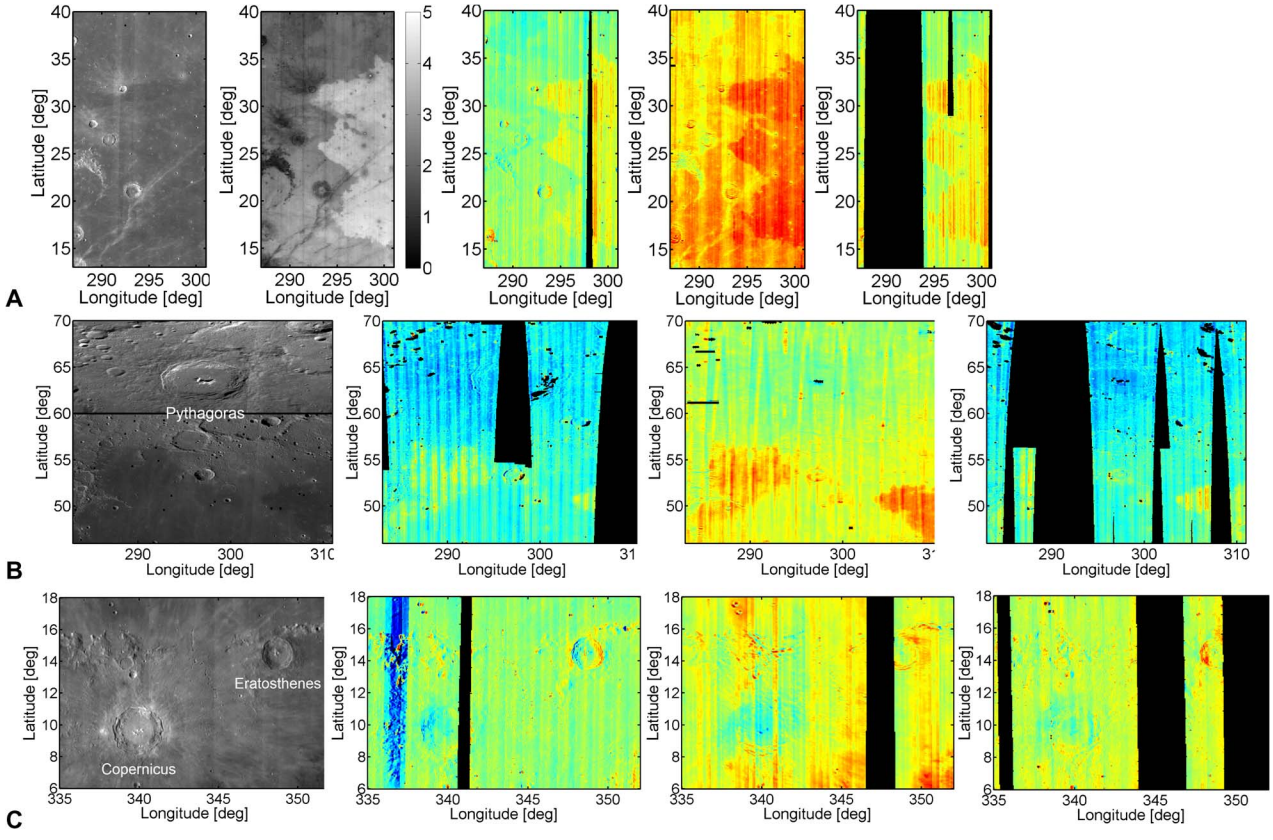

Fig. 3. Regional OHIBD maps. (**A**) Boundary between high- and low-Ti mare basalts in western Oceanus Procellarum: Excerpt from LRO Camera (LROC) Wide-Angle Camera (WAC) mosaic (*51*), M^3-based Ti wt % abundance map obtained with the method of Bhatt *et al.* (*25*), and OHIBD maps (morning, midday, and afternoon). (**B**) Boundary between mare and highland areas south of the crater Pythagoras: Excerpt from LROC WAC mosaic (*51*) and OHIBD maps (morning, midday, and afternoon). (**C**) Region around the craters Copernicus and Eratosthenes: Excerpt from LROC WAC mosaic (*51*) and OHIBD maps (morning, midday, and afternoon) (color coding as in Fig. 2).

Time-of-day–dependent global and regional OHIBD maps

The OHIBD maps for morning, midday, and evening illumination are shown in Fig. 2. Given the range of wavelengths used for OHIBD estimation (2697 to 2936 nm), the OHIBD values mainly characterize the behavior of the OH absorption band at 2.82 μm, but H_2O also has some influence on the OHIBD values because the 2.95-μm H_2O band overlaps with that wavelength range as well.

In the lunar morning (07:00 to 08:00 in Fig. 2), the OHIBD in the illuminated polar highlands is higher by 20 to 30% than in the equatorial highlands. Near the equator, a clearly nonzero highland OHIBD level can be observed. The OHIBD in the lunar maria is lower by 10 to 15% than in the equatorial highlands, where the lowest OHIBD values are found for the high-Ti mare basalts, such as Mare Tranquillitatis and western Oceanus Procellarum [see, for example, the study by Lucey *et al.* (*24*) or Bhatt *et al.* (*25*) for lunar Ti abundance maps]. In the lunar morning, the highest OHIBD level in mare areas can be found in Mare Crisium, Mare Nectaris, and Mare Serenitatis. At lunar midday (12:00 to 14:00 on the nearside and 10:00 to 12:00 on the farside in Fig. 2), there is no obvious latitude dependence of the OHIBD. The OHIBD level in the equatorial highlands is about 10 to 15% lower than in the morning. In the lunar maria, low OHIBD values can be observed, where the maximal level is found in Mare Crisium, Mare Serenitatis, and Mare Nectaris, and the lowest level is found in the high-Ti basalts of Mare Tranquillitatis, northeastern Mare Fecunditatis, central Mare Imbrium, and western Oceanus Procellarum. In the lunar evening (16:00 to 17:00 in Fig. 2), the OHIBD difference between the equatorial and the polar highlands is similar to that in the morning. The highland OHIBD level is similar as that in the morning, whereas the mare OHIBD level is higher than that at midday, but about 20% lower than that in the morning. The lowest OHIBD values are mainly found in the high-Ti mare basalts of Mare Imbrium and Oceanus Procellarum. The time-of-day–dependent OHIBD behavior for two selected regions, exhibiting a boundary between high- and low-Ti mare basalts and a boundary between mare and highland areas, respectively, is shown in Fig. 3.

The relative OHIBD decrease in the illuminated polar highlands between morning and midday corresponds to ~30%, whereas the low-latitude highlands exhibit a nearly constant, nonzero OHIBD level. Relatively small time-of-day–dependent OHIBD variations of ~20% are found in Mare Crisium, Mare Nectaris, Mare Serenitatis, and the South Pole–Aitken basin. In the high-Ti basalts of Mare Tranquillitatis and central Mare Imbrium, the time-of-day–dependent relative OHIBD variations are much larger and correspond to ~50 to 70%. In the highlands, the time-of-day–dependent OHIBD behavior is symmetric with respect to midday, whereas it is slightly asymmetric in the lunar maria with a difference of ~20% between the OHIBD level in the morning and evening, that is, 1 to 2 lunar hours after sunrise and before sunset, respectively. In regions at low latitudes illuminated obliquely in the morning and evening, surface parts inclined toward the sun, thus being warmer than even surface parts, exhibit higher OHIBD values, whereas colder surface parts inclined away from the sun have a lower OHIBD compared to even surfaces (Fig. 3). A similar behavior is apparent in the evening.

However, this topography dependence of the OHIBD can only be clearly observed for steep slopes that occur particularly in the walls of not strongly degraded craters, such as Copernicus and Eratosthenes (Fig. 3).

DISCUSSION

Comparison with previous results

The presented observations of the time-of-day–dependent OHIBD are in contrast to the previous results of Pieters *et al.* (*2*), where the H_2O/OH absorption depth is found to be zero at latitudes below about 50° in both mare and highland regions. The most likely reason for this discrepancy is that the results in the study by Pieters *et al.* (*2*) were obtained with the thermal emission removal technique of Clark (*26*), which can be considered a predecessor of Clark *et al.* (*14*). In contrast to our thermal emission removal approach (*5*), the methods of Clark *et al.* (*14*) and Clark (*26*) are based on specific assumptions about the shape of the reflectance spectrum. Regarding the effect of local topography near the equator under oblique illumination, a strong inverse correlation between solar irradiance and H_2O/OH absorption depth is found in the study by McCord *et al.* (*3*) without performing a thermal emission removal. This result of McCord *et al.* (*3*) contradicts our observation of a (typically weak) positive correlation between solar irradiance and OHIBD at low latitudes in the lunar morning and evening.

In principle, it may be possible that the observed time-of-day–dependent OHIBD variations can, in part, be attributed to the varying time-of-day–dependent surface temperatures. For example, spectroscopic analyses of asteroids indicate that the width of the broad absorption band of olivine around 1-μm wavelength increases significantly with increasing temperature in the range of 83 to 448 K (*27*). A similar variation of the absorption band width around 2-μm wavelength is demonstrated in the study by Hinrichs and Lucey (*28*) for orthopyroxene in the temperature range of 100 to 400 K. Spectral analyses of ordinary and carbonaceous chondrite meteorites, as well as eucrite and howardite samples, show a considerable temperature dependence of the depth and position of the absorption bands near 1 and 2 μm in the temperature range of 80 to 400 K (*28*). However, the dependence of the spectrum of a lunar sample in the same temperature range is shown in the study by Hinrichs and Lucey (*28*) to be very weak. Analysis of the temperature dependence of the depth, width, and integrated depth of several absorption bands of hexagonal H_2O ice (however, not including the 3-μm absorption band) reveals strong temperature effects on all three band parameters in the range of 20 to 270 K (*29*). At the lunar equator, the surface temperature differences between the M^3 morning/afternoon and midday observations may exceed 100 K. However, at high latitudes, the OHIBD variations are stronger than near the equator, whereas the surface temperature differences are only a few tens of kelvin between morning and midday observations [for example, about 20 K on even surface at 73°S (*5*)] and thus much smaller than the temperature ranges analyzed in the study by Lucey *et al.* (*27*), Hinrichs and Lucey (*28*), and Grundy and Schmitt (*29*). Hence, it is unlikely that the changing surface temperature has a major direct effect on the time-of-day–dependent OHIBD variations.

Possible source and sink mechanisms for surficial water/OH

A commonly assumed mechanism for explaining the occurrence of the lunar 3-μm H_2O/OH absorption band is the adsorption of protons from the solar wind by the regolith and the subsequent reaction with oxygen bounded in the regolith material, leading to the formation of surficial H_2O/OH [for example, see previous studies (*2*, *3*, *30*–*32*)]. A steady-state approach to estimate the atomic hydrogen (H) content in the uppermost few 10^{-8} m of the lunar regolith is proposed in the study by Farrell *et al.* (*32*), taking into account the adsorption of solar wind protons as a H source and temperature-dependent diffusion (evaporation) as a H sink [reactions between H and O atoms as an additional H sink (*31*) are not considered]. The equilibrium condition for the validity of the stationary solution obtained in the study by Farrell *et al.* (*32*) is met best at lunar midday, when the illumination angle and, thus, the solar wind intensity and the surface temperature change only slowly. At midday, the steady-state approach of Farrell *et al.* (*32*) predicts the density of adsorbed H at 70° latitude to be three times higher than the H density at the equator. Although this does not necessarily translate into the same relation between the OH densities at 70° and 0° latitude, it is clearly inconsistent with the OHIBD being largely latitude-independent at midday (Fig. 4). In addition, the clearly nonzero equatorial highland OHIBD level at midday and the weak time-of-day–dependent OHIBD variations in the equatorial highlands do not support the assumption of adsorption of solar wind protons as the sole source of the 3-μm H_2O/OH absorption band. Furthermore, the steady-state model of Farrell *et al.* (*32*) predicts an absolute H fraction of only a few tenths of parts per million (ppm) at midday for latitudes below 60°, which is much less than the range of H abundances between about 1 and 100 ppm (10- to 1000-ppm H_2O) found on the basis of near-infrared spectroscopy in the study by Clark (*33*).

Here, one might consider the presence of a more strongly bounded H_2O/OH component (*17*, *34*) in the uppermost regolith surface, which is not subject to diffusion/thermal evaporation or photolysis, thus providing

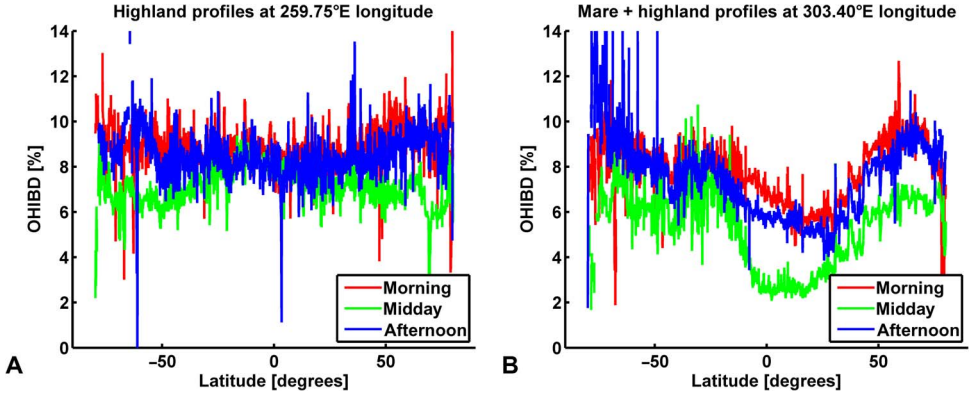

Fig. 4. OHIBD longitudinal profiles. (**A**) Highland surface west of Oceanus Procellarum. (**B**) Mare (western Oceanus Procellarum) and highland surface.

a "background signal," which is stronger for highland than for mare surfaces. The observed OHIBD behavior could then be explained by the additive effect of the constant strongly bounded component plus a time-of-day–dependent variable component governed by the competing processes of H adsorption from the solar wind (*3*, *30*–*32*), diffusion/thermal evaporation of H, OH, and H_2O (*5*, *30*–*32*), photolysis of OH and H_2O (*5*, *31*, *35*), and reactions between H and O atoms (*31*). The relative importance of these mechanisms depends on a variety of factors such as solar illumination conditions, surface reflectance, surface temperature, and kinetic properties of the involved chemical reactions. For example, the generally lower OHIBD level in the lunar maria compared to the highlands might be explained by higher surface temperatures in the lunar maria due to their lower albedo, leading to a stronger OH diffusion. Similarly, the observation of increased OHIBD values on more steeply illuminated warmer slopes of not strongly degraded impact craters may be explained such that for these surfaces shortly after sunrise and before sunset, the adsorption of H supersedes the loss of H_2O/OH caused by diffusion/thermal evaporation and photolysis.

One might expect systematic OHIBD differences between the nearside and farside at midday due to the influence of Earth's magnetotail plasma, because the Moon is located inside Earth's magnetotail for a period of time of about 1 week around full Moon (*9*). The interactions between the magnetotail plasma and the lunar surface are of highly complex nature (*36*). Figure 2B indicates that the midday OHIBD in the nearside southern highlands around 0° longitude is lower by ~10 to 20% than the midday OHIBD in the northern farside highlands around 180° longitude (outside the South Pole–Aitken basin). However, this observation should not be overinterpreted because the nearside highlands are more strongly contaminated by material from nearby mare regions than farside highlands and have a slightly more mafic composition (*37*), which may result in a reduced OHIBD level. Further differences between southern nearside and northern farside highlands may be due to the presence of the ray system of the prominent crater Tycho in the southern nearside highlands around the 0° meridian. These compositional effects might also be an explanation for the observed difference in the OHIBD level. Besides, the study Starukhina and Shkuratov (*9*) states that the proton flux at the lunar surface is similar during exposition to the solar wind and when the Moon is located inside Earth's magnetotail, which would rather predict an absence of systematic nearside versus farside OHIBD differences at lunar midday.

All in all, our results suggest that the observed near-infrared spectral signature of lunar surficial H_2O/OH can be explained by a combined mechanism involving the presence of endogenous H_2O/OH strongly bounded by the lunar regolith, as well as processes and reactions induced by the adsorption of protons from the solar wind by the regolith material.

MATERIALS AND METHODS

Surface temperature estimation

Our M^3 data processing framework relies on the level 1B spectral radiance image data published on the PDS (*13*), which we resampled to a resolution of 20 pixels per degree (about 1.5 km at the lunar equator). The measured spectral radiance is a superposition of a reflected component and a thermal emission component, where the latter has to be subtracted from the radiance spectrum before any further analysis. This step requires the accurate estimation of the surface temperature and the spectral emissivity. The approach used in this work closely follows the method of Shkuratov *et al.* (*18*), where according to the assumption of thermal equilibrium and a smooth surface, the local surface temperature T is given by

$$T = T_0 \sqrt[4]{(1 - A_{\mathrm{dh}}) \cos i} \tag{1}$$

where i is the solar incidence angle, A_{dh} is the spectrally integrated directional hemispherical albedo, and T_0 is the temperature of a perfectly absorbing surface perpendicularly illuminated by the sun. For 1–astronomical unit solar distance, it is $T_0 = 394$ K (*18*). The value of A_{dh} depends on the well-known solar spectral irradiance and the directional-hemispherical spectral reflectance of the surface, which can be inferred from the bidirectional spectral reflectance, as shown in the study by Shkuratov *et al.* (*18*), where in this work, the Hapke model (*19*, *20*) was used for reflectance modeling, that is, the single-scattering albedo of the Hapke model was adapted to the measured bidirectional M^3 reflectances. The wavelength integral was then separated into three ranges. In the range of 461 to 2936 nm, we used the M^3-derived reflectance model to evaluate the directional-hemispherical reflectance as defined by Hapke (*20*, *38*). Because the reflectance shows a monotonously increasing behavior, a second-order polynomial is adapted to the M^3-derived reflectance. In the range of 250 to 461 nm, the measured M^3 spectral reflectance was extrapolated using this polynomial. The spectral reflectance is well known to drop to low values at longer wavelengths. We thus used a constant approximation of 0.016 for the directional-hemispherical reflectance in the range of 3000 to 17,000 nm. Beyond 17,000 nm, the solar spectral irradiance has been neglected. Eventually, A_{dh} was computed using a numerical integration for each of the three wavelength ranges, respectively.

According to Shkuratov *et al.* (*18*), the wavelength-dependent spectral emissivity is

$$\varepsilon(\lambda) = 1 - r_{\mathrm{hd}}(\lambda) \tag{2}$$

which follows Kirchhoff's law and has been confirmed experimentally, for example, by Arpin *et al.* (*39*). In Eq. 2, $r_{\mathrm{hd}}(\lambda)$ is the hemispherical-directional reflectance at wavelength λ, as defined by Shkuratov *et al.* (*18*) and Hapke (*38*). The thermal emission component resulting from a black body of the surface temperature T was multiplied by the M^3-derived spectral emissivity $\varepsilon(\lambda)$ and subtracted from the spectral radiance. The solar irradiance is weak in the range of 3000 to 17,000 nm, and thus, a variation of the assumed constant spectral reflectance value beyond 3000 nm by 0.1 has a negligible effect on A_{dh} and thus only results in a change in surface temperature of the order 10^{-1} K.

A division of the thermally corrected radiance spectrum by the solar irradiance spectrum yields the bidirectional reflectance spectrum. Because the reflectance depends on the surface temperature T, an initial value of T was computed by adapting a superposition of a standard reflectance spectrum and a black body emission spectrum of temperature T to the M^3 data (*40*). On the basis of this initial value, the reflectance was derived, and a surface temperature was computed according to Eq. (1), which, in turn, allows for computing refined values of $r_{\mathrm{hd}}(\lambda)$, $\varepsilon(\lambda)$, A_{dh}, and T. Thus, T and $\varepsilon(\lambda)$ were estimated simultaneously. This procedure is iterated until the average temperature change per iteration cycle falls below 0.001 K. Hence, our approach ensures that, for all wavelengths within the M^3 spectral range, exactly the spectral emissivity that follows from the measured reflectance spectrum was used for thermal emission removal in a self-consistent manner.

In particular, when the illumination of the surface is oblique, an additional factor that has a strong effect on the surface temperature is the roughness of the surface (*7*). Because of the low thermal conductivity of

the lunar regolith, surface facets inclined away from the sun may be much colder than nearby surface facets inclined toward the sun, such that the surface area covered by an image pixel cannot be described by one single temperature value but rather by a superposition of black bodies with different temperatures (*7*, *16*). In the study by Davidsson *et al.* (*16*), random surfaces are constructed on the basis of four basic shapes: concave spherical segments, parallel sinusoidal trenches, random Gaussians, and fractals. The first two approaches do not involve random shapes, and the parameters of the basic shapes are chosen such that the desired root mean square (RMS) slope is obtained. For the random Gaussian method of Davidsson *et al.* (*16*), an increasing number of two-dimensional Gaussians with randomly chosen heights, widths, and positions are superposed until the desired RMS slope is obtained. In the fractals method of Davidsson *et al.* (*16*), the height-scale parameter of an algorithm that generates fractal surfaces is adjusted until the desired RMS slope is obtained. In contrast, we used the Fourier transform–based method of Muinonen and Saarinen (*41*) and Lagerros (*42*), which generates a random surface with a Gaussian autocorrelation and a Gaussian distribution of the normal directions of the surface facets, given the user-defined RMS slope. A summary of this method can be found in the appendix of Wöhler *et al.* (*5*). The approach of Davidsson *et al.* (*16*) which is most similar to the method of Muinonen and Saarinen (*41*) and Lagerros (*42*), is the fractals technique because both yield surfaces with facets having a Gaussian distribution of surface normal orientations. An RMS slope of 9° is found in the study by Wöhler *et al.* (*5*) based on a comparison of the spatial scale of thermal equilibrium in the lunar regolith with the three-dimensional regolith maps of Helfenstein and Shepard (*43*) constructed using in situ close-range stereo photograph.

For computing $r_{hd}(\lambda)$, $\varepsilon(\lambda)$, and A_{dh}, the spectral behavior of lunar surface materials was modeled using reflectance spectra from the catalog of the Lunar Soil Characterization Consortium (*22*, *23*). The thermal equilibrium–based surface temperature estimation approach was then applied to each surface facet, and the thermal emission spectrum of the rough surface was determined by summing up the individual emitted radiance spectra of all facets.

Although this summed emission spectrum is composed of the emission spectra of many black bodies of different temperatures, for the temperature range encountered on the lunar surface and wavelengths less than 3000 nm (roughly the upper limit of the M^3 wavelength range), a close approximation across the wavelength range shortward of 3 μm by the emission spectrum of a single black body with an effective temperature T_{eff} is possible, as shown in Fig. 5. The differences between T_{eff} and the temperature T of a smooth surface with the same spectral behavior illuminated at the same incidence angle were stored as a correction function depending on the average surface albedo and the incidence angle (*5*). The final correction of the M^3 level 1B radiance data for thermal emission was then performed on the basis of the obtained pixel-wise spectral emissivity $\varepsilon(\lambda)$ and effective temperature T_{eff}.

The RMS slope has been derived in the study by Bandfield *et al.* (*7*) by comparison between modeled temperatures and data of the LRO Diviner instrument, relying on four equatorial locations situated at latitudes less than 6°. For equatorial morning and afternoon local times shortly after 06:00 and shortly before 18:00, an RMS slope of 5° to 10° has been obtained in the study by Bandfield *et al.* (*7*), whereas around midday (09:00 to 15:00), the estimated RMS slope is larger and corresponds to 20° (*7*). Because the RMS slope is a purely geometric quantity, this dependence of RMS slope on incidence angle is unexpected. However, at the small incidence angles at lunar midday, the roughness-related brightness temperature differences modeled in the study by Bandfield *et al.* (*7*) are nearly independent of the RMS slope, at least the analysis in the study by Bandfield *et al.* (*7*) shows that this is the case around 10:00 to 14:00 local time, where the results of the 10° RMS slope model fit similarly well with the observations as the results of the 20° RMS slope model, given the measurement scatter. Hence, at illumination angles under which the assumed value of the RMS slope has a significant effect on the surface temperature and thus on the H_2O/OH absorption band depth, that is, at high latitudes and in the equatorial morning and afternoon, the RMS slope inferred by Bandfield *et al.* (*7*) is largely consistent with our assumed value of 9°. Only at those illumination angles where the influence of the RMS slope is weak, our assumed RMS slope is smaller than the value derived in the study by Bandfield *et al.* (*7*).

To illustrate the effect of different RMS slope angles on our global OHIBD maps, we have included additional global OHIBD maps for RMS slopes of 0° and 20° in the Supplementary Materials. For high incidence angles, the effective surface temperature T_{eff} exceeds the temperature T of an identically illuminated smooth surface, and the difference ($T_{eff} - T$) increases with increasing RMS slope (*5*). The strength of the H_2O/OH absorption band then increases with increasing RMS slope. In this case, all facets of a smooth surface are illuminated at an identically high incidence angle. For a rough surface, the distribution of facet normals causes half of the facets to be illuminated more steeply than a rough surface (thus to become warmer than a smooth surface) and the other half to be illuminated more obliquely (thus to become less warm than a smooth surface). Because of the strong increase in the thermal emission

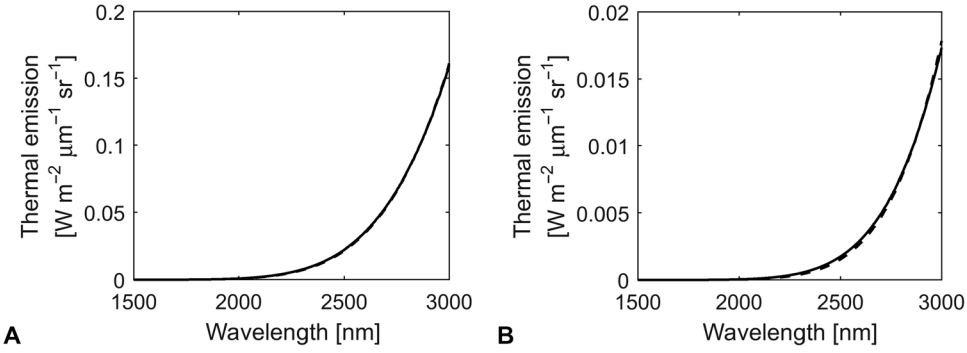

Fig. 5. Comparison between the thermal emission spectrum of a surface with RMS slope of 9° (solid line) and the thermal emission of a single black body with the best-fitting effective temperature T_{eff} (dashed line). (**A**) Incidence angle 60°. (**B**) Incidence angle 75°. The emissivity was computed on the basis of the reflectance spectrum of lunar highland sample 62231 (*23*).

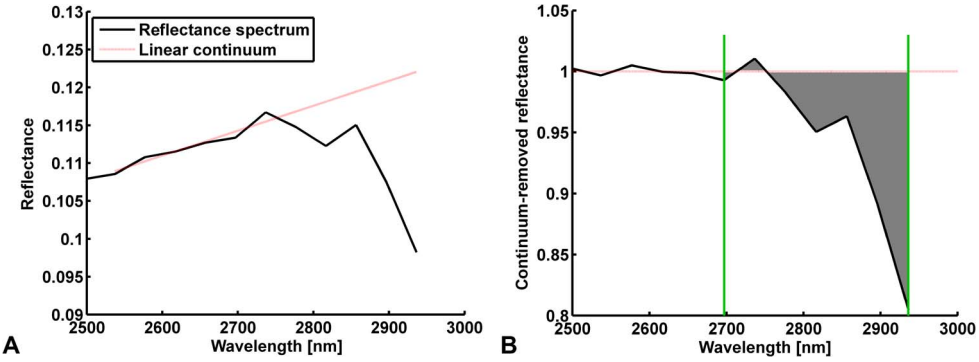

Fig. 6. Definition of the OHIBD parameter. (**A**) Part of a typical M^3 reflectance spectrum (12.64°E, 20.00°N; local time, 12:45) longward of 2500 nm with linear continuum fitted to the wavelength range of 2537 to 2657 nm. (**B**) Continuum-removed spectrum obtained by division of the reflectance spectrum by the continuum. The integral between M^3 channels 78 and 84 (2697 to 2936 nm) of the continuum-removed spectrum subtracted from 1 is shown in gray.

with the fourth power of the surface temperature, the effect of the more steeply illuminated facets supersedes that of the more obliquely illuminated facets, leading to $T_{eff} > T$ and increasing H_2O/OH absorption band depth with increasing RMS slope. In contrast, for low incidence angles, T_{eff} is slightly lower than T (*5*), such that at low latitudes at midday, the H_2O/OH absorption band depth decreases with increasing RMS slope. In this case, for a smooth surface, all facet normals have the same small incidence angle. In contrast, for a rough surface, the distribution of facet normals causes some facets to be illuminated steeply, thus having temperatures similar to T, whereas many facets are illuminated at higher incidence angles, thus having temperatures below T, leading to $T_{eff} < T$.

All in all, the maps in figs. S1 and S2 show that the global properties of the OHIBD, especially its latitude dependence at different times of day, remain the same, independent of the actually assumed RMS slope. Thus, the results described in this paper do not critically depend on the assumed specific value of the RMS slope angle.

Photometric correction

Because the spectral reflectance depends on the pixel-specific incidence and emission angles, it is necessary to correct the reflectance spectra photometrically, that is, to normalize them to a uniform illumination and observation geometry to allow for a direct comparison between spectra. To determine the local, topography-dependent incidence and emission angles, we used the GLD100 lunar topographic map (*21*). The GLD100 is well suitable for this purpose because it is mentioned in the study by Scholten *et al.* (*21*) that the smallest structures reliably recoverable in it have a size of about 1.5 km, corresponding to the resolution of the resampled M^3 spectral radiance data. The pixel-specific incidence and emission angles were then determined on the basis of the solar illumination vector and the spacecraft observation vector published on the PDS for each M^3 image pixel and the surface normal vector inferred from the GLD100. On the basis of the spectral reflectance and the incidence and emission angle, the spectrum of the single scattering albedo was computed based on the Hapke model (*19*, *20*). The model parameters besides the single-scattering albedo, that is, the two parameters of the double Henyey-Greenstein single-particle scattering function (*20*), the strength and width of the opposition effect [(*20*); see also the study by Shkuratov *et al.* (*44*)], and the photometric roughness parameter (*19*), are adopted from the first lunar solution by Warell (*45*). The uniform illumination and observation geometry of 30° incidence angle and 0° emission angle (*46*) was then inserted into the Hapke model to compute the normalized reflectance spectrum, which has been used for all analyses of this work. There exists a so-called "ground truth correction" (*47*, *48*), which we have not applied to the level 1B spectral radiance data. It corrects for the effects of different detector temperatures. The correction consists of a wavelength-dependent correction factor that was designed to recover the shape of the 1-μm absorption band of mature lunar soils. This correction factor was derived from an analysis of the continuum-removed M^3 spectra and a reference laboratory spectrum (*47*). However, the ground truth correction has been designed to not interfere with the spectral reflectance in the range of 2500 to 3000 nm (*47*). It is thus not relevant for this study and is not discussed further. For more detailed information about the M^3 data processing framework, see previous studies (*5*, *40*, *49*, *50*).

The midday OHIBD maps in Figs. 2 and 3 show strip-like artifacts in the north-south direction. They are not due to OHIBD variations from one M^3 image to the other but result from OHIBD gradients within individual M^3 images in cross-track direction. Our photometric correction is based on the full Hapke model (*19*, *20*) without simplification. Of course, the Hapke model parameters might exhibit local deviations from the assumed global values of Warell (*45*), but the strip-like artifacts occur at midday at all latitudes and for both lunar maria and highlands. We, thus, assume that the artifacts may likely be caused by detector-specific effects such as detector temperature–dependent inaccuracies of the M^3 flat-field correction.

Definition of the OHIBD

The definition of the OHIBD used as a measure of the H_2O/OH band depth is illustrated in Fig. 6. A linear continuum was fitted to the normalized reflectance spectrum over M^3 channels 74 to 77 (2537 to 2657 nm) (Fig. 6A). Division of the reflectance spectrum by this continuum yields the continuum-removed reflectance spectrum (Fig. 6B). Then, the integral of the continuum-removed spectrum subtracted from 1 between M^3 channels 78 and 84 (2697 to 2936 nm) was computed (shown as gray area in Fig. 6B), where contributions below and above the dotted red line were counted as positive and negative, respectively. The OHIBD is defined as the fraction between this integral and the rectangular area under the dotted red line in Fig. 6B from 2697 to 2936 nm, that is

$$\mathrm{OHIBD} = \left[\int_{\lambda_{min}}^{\lambda_{max}} \left(1 - \frac{R(\lambda)}{c(\lambda)}\right) d\lambda\right] / [\lambda_{max} - \lambda_{min}] \qquad (3)$$

where $\lambda_{min} = 2697$ nm, $\lambda_{max} = 2936$ nm, $R(\lambda)$ is the bidirectional spectral reflectance, and $c(\lambda)$ is the linear continuum fitted to the wavelength range of 2537 to 2657 nm. The OHIBD can, thus, be interpreted as an

average relative absorption strength across the wavelength interval of 2697 to 2936 nm.

SUPPLEMENTARY MATERIALS

Supplementary material for this article is available at http://advances.sciencemag.org/cgi/content/full/3/9/e1701286/DC1

fig. S1. Global OHIBD maps in orthographic projection (0° RMS slope).

fig. S2. Global OHIBD maps in orthographic projection (20° RMS slope).

REFERENCES AND NOTES

1. C. M. Pieters, J. Boardman, B. Buratti, A. Chatterjee, R. Clark, T. Glavich, R. Green, J. Head, P. Isaacson, E. Malaret, T. McCord, J. Mustard, N. Petro, C. Runyon, M. Staid, J. Sunshine, L. Taylor, S. Tompkins, P. Varanasi, M. White, The Moon mineralogy mapper (M^3) on Chandrayaan-1. *Curr. Sci.* **96**, 500–505 (2009).
2. C. M. Pieters, J. N. Goswami, R. N. Clark, M. Annadurai, J. Boardman, B. Buratti, J.-P. Combe, M. D. Dyar, R. Green, J. W. Head, C. Hibbitts, M. Hicks, P. Isaacson, R. Klima, G. Kramer, S. Kumar, E. Livo, S. Lundeen, E. Malaret, T. McCord, J. Mustard, J. Nettles, N. Petro, C. Runyon, M. Staid, J. Sunshine, L. A. Taylor, S. Tompkins, P. Varanasi, Character and spatial distribution of OH/H_2O on the surface of the Moon seen by M^3 on Chandrayaan-1. *Science* **326**, 568–572 (2009).
3. T. B. McCord, L. A. Taylor, J.-P. Combe, G. Kramer, C. M. Pieters, J. M. Sunshine, R. N. Clark, Sources and physical processes responsible for OH/H_2O in the lunar soil as revealed by the Moon Mineralogy Mapper (M^3). *J. Geophys. Res.* **116**, E00G05 (2011).
4. J. M. Sunshine, T. L. Farnham, L. M. Feaga, O. Groussin, F. Merlin, R. E. Milliken, M. F. A'Hearn, Temporal and spatial variability of lunar hydration as observed by the Deep Impact spacecraft. *Science* **326**, 565–568 (2009).
5. C. Wöhler, A. Grumpe, A. A. Berezhnoy, E. A. Feoktistova, N. A. Evdokimova, K. Kapoor, V. V. Shevchenko, Temperature regime and water/hydroxyl behavior in the crater Boguslawsky on the Moon. *Icarus* **285**, 118–136 (2017).
6. J. L. Bandfield, M. J. Poston, R. L. Klima, C. S. Edwards, A prominent and ubiquitous OH/H_2O feature in corrected lunar spectra. *Proc. Lunar Planet. Sci.* **XLVIII**, abstract no. 2083 (2017).
7. J. L. Bandfield, P. O. Hayne, J.-P. Williams, B. T. Greenhagen, D. A. Paige, Lunar surface roughness derived from LRO Diviner Radiometer observations. *Icarus* **248**, 357–372 (2015).
8. W. C. Feldman, S. Maurice, A. B. Binder, B. L. Barraclough, R. C. Elphic, D. J. Lawrence, Fluxes of fast and epithermal neutrons from Lunar Prospector: Evidence for water ice at the lunar poles. *Science* **281**, 1496–1500 (1998).
9. L. V. Starukhina, Y. G. Shkuratov, The Lunar Poles: Water ice or chemically trapped hydrogen? *Icarus* **147**, 585–587 (2000).
10. A. B. Sanin, I. G. Mitrofanov, M. L. Litvak, B. N. Bakhtin, J. G. Bodnarik, W. V. Boynton, G. Chin, L. G. Evans, K. Harshman, F. Fedosov, D. V. Golovin, A. S. Kozyrev, T. A. Livengood, A. V. Malakhov, T. P. McClanahan, M. I. Mokrousov, R. D. Starr, R. Z. Sagdeev, V. I. Tret'yakov, A. A. Vostrukhin, Hydrogen distribution in the lunar polar regions. *Icarus* **283**, 20–30 (2017).
11. T. P. McClanahan, I. G. Mitrofanov, W. V. Boynton, G. Chin, J. Bodnarik, G. Droege, L. G. Evans, D. Golovin, D. Hamara, K. Harshman, M. Litvak, T. A. Livengood, A. Malakhov, E. Mazarico, G. Milikh, G. Nandikotkur, A. Parsons, R. Sagdeev, A. Sanin, R. D. Starr, J. J. Su, J. Murray, Evidence for the sequestration of hydrogen-bearing volatiles towards the Moon's southern pole-facing slopes. *Icarus* **255**, 88–99 (2015).
12. T. A. Livengood, G. Chin, R. Z. Sagdeev, I. G. Mitrofanov, W. V. Boynton, L. G. Evans, M. L. Litvak, T. P. McClanahan, A. B. Sanin, R. D. Starr, J. J. Su, Moonshine: Diurnally varying hydration through natural distillation on the Moon, detected by the Lunar Exploration Neutron Detector (LEND). *Icarus* **255**, 100–115 (2015).
13. Planetary Data System (PDS) (2017); http://pds-imaging.jpl.nasa.gov/volumes/m3.html.
14. R. N. Clark, C. M. Pieters, R. O. Green, J. W. Boardman, N. E. Petro, Thermal removal from near-infrared imaging spectroscopy data of the Moon. *J. Geophys. Res.* **116**, E00G16 (2011).
15. P. Isaacson, S. Besse, N. Petro, J. Nettles; M^3 Team, "M^3 overview and working with M^3 data" (Technical Report, 2011); http://pds-imaging.jpl.nasa.gov/documentation/Isaacson_M3_Workshop_Final.pdf.
16. B. J. R. Davidsson, H. Rickman, J. L. Bandfield, O. Groussin, P. J. Gutiérrez, M. Wilska, M. T. Capria, J. P. Emery, J. Helbert, L. Jorda, A. Maturilli, T. G. Mueller, Interpretation of thermal emission. I. The effect of roughness for spatially resolved atmosphereless bodies. *Icarus* **252**, 1–21 (2015).
17. J. L. Bandfield, C. S. Edwards, M. J. Poston, R. L. Klima, Lunar H_2O/OH- distributions: Revised infrared spectra from improved thermal corrections. *Proc. Lunar Planet. Sci.* **XXXXVII**, abstract no. 1594 (2016).
18. Y. Shkuratov, V. Kaydash, V. Korokhin, Y. Velikodsky, N. Opanasenko, G. Videen, Optical measurements of the Moon as a tool to study its surface. *Planet. Space Sci.* **59**, 1326–1371 (2011).
19. B. Hapke, Bidirectional reflectance spectroscopy: 3. Correction for macroscopic roughness. *Icarus* **59**, 41–59 (1984).
20. B. Hapke, Bidirectional reflectance spectroscopy: 5. The coherent backscatter opposition effect and anisotropic scattering. *Icarus* **157**, 523–534 (2002).
21. F. Scholten, J. Oberst, K.-D. Matz, T. Roatsch, M. Wählisch, E. J. Speyerer, M. S. Robinson, GLD100: The near-global lunar 100 m raster DTM from LROC WAC stereo image data. *J. Geophys. Res.* **117**, E00H17 (2012).
22. L. A. Taylor, C. M. Pieters, L. P. Keller, R. V. Morris, D. S. McKay, Lunar Mare Soils: Space weathering and the major effects of surface-correlated nanophase Fe. *J. Geophys. Res.* **106**, 27985–27999 (2001).
23. L. A. Taylor, C. Pieters, A. Patchen, D.-H. S. Taylor, R. V. Morris, L. P. Keller, D. S. McKay, Mineralogical and chemical characterization of lunar highland soils: Insights into the space weathering of soils on airless bodies. *J. Geophys. Res.* **115**, E02002 (2010).
24. P. G. Lucey, D. T. Blewett, B. L. Jolliff, Lunar iron and titanium abundance algorithms based on final processing of Clementine ultraviolet-visible images. *J. Geophys. Res.* **105**, 20297–20305 (2000).
25. M. Bhatt, U. Mall, C. Wöhler, A. Grumpe, R. Bugiolacchi, A comparative study of iron abundance estimation methods: Application to the western nearside of the Moon. *Icarus* **248**, 72–88 (2015).
26. R. N. Clark, Planetary reflectance measurements in the region of planetary thermal emission. *Icarus* **40**, 94–103 (1979).
27. P. G. Lucey, K. Keil, R. Whitely, The influence of temperature on the spectra of the A-asteroids and implications for their silicate chemistry. *J. Geophys. Res.* **103**, 5865–5871 (1998).
28. J. L. Hinrichs, P. G. Lucey, Temperature-dependent near-infrared spectral properties of minerals, meteorites, and lunar soil. *Icarus* **155**, 169–180 (2002).
29. W. M. Grundy, B. Schmitt, The temperature-dependent near-infrared absorption spectrum of hexagonal H_2O ice. *J. Geophys. Res.* **103**, 25809–25822 (1998).
30. L. Starukhina, Water detection on atmosphereless celestial bodies: Alternative explanations of the observations. *J. Geophys. Res.* **106**, 14701–14710 (2001).
31. W. M. Farrell, D. M. Hurley, M. I. Zimmerman, Solar wind implantation into lunar regolith: Hydrogen retention in a surface with defects. *Icarus* **255**, 116–126 (2015).
32. W. M. Farrell, D. M. Hurley, V. J. Esposito, J. L. McLain, M. I. Zimmerman, The statistical mechanics of solar wind hydroxylation at the Moon, within lunar magnetic anomalies, and at Phobos. *J. Geophys. Res.* **122**, 269–289 (2017).
33. R. N. Clark, Detection of adsorbed water and hydroxyl on the Moon. *Science* **326**, 562–564 (2009).
34. A. E. Saal, E. H. Hauri, M. L. Cascio, J. A. Van Orman, M. C. Rutherford, R. F. Cooper, Volatile content of lunar volcanic glasses and the presence of water in the Moon's interior. *Nature* **454**, 192–195 (2008).
35. E. H. Mitchell, U. Raut, D. Fulvio, M. J. Schaible, C. A. Dukes, R. A. Baragiola, Ultraviolet photodesorption as a driver of water migration on the lunar surface. *Planet. Space Sci.* **89**, 42–46 (2013).
36. A. Bhardwaj, M. B. Dhanya, A. Alok, S. Barabash, M. Wieser, Y. Futaana, P. Wurz, A. Vorburger, M. Holmström, C. Lue, Y. Harada, K. Asamura, A new view on the solar wind interaction with the Moon. *Geosci. Lett.* **2**, 10 (2015)
37. P. G. Lucey, Mineral maps of the Moon. *Geophys. Res. Lett.* **31**, L08701 (2004).
38. B. Hapke, *Theory of Reflectance and Emittance Spectroscopy* (Cambridge Univ. Press, 2012).
39. K. A. Arpin, M. D. Losego, A. N. Cloud, H. Ning, J. Mallek, N. P. Sergeant, L. Zhu, Z. Yu, B. Kalanyan, G. N. Parsons, G. S. Girolami, J. R. Abelson, S. Fan, P. V. Braun, Three-dimensional self-assembled photonic crystals with high temperature stability for thermal emission modification. *Nat. Commun.* **4**, 2630 (2013).
40. C. Wöhler, A. Grumpe, A. Berezhnoy, M. U. Bhatt, U. Mall, Integrated topographic, photometric and spectral analysis of the lunar surface: Application to impact melt flows and ponds. *Icarus* **235**, 86–122 (2014).
41. K. Muinonen, K. Saarinen, Ray optics approximation for Gaussian random cylinders. *J. Quant. Spectrosc. Radiat. Transfer* **64**, 201–218 (2000).
42. J. S. V. Lagerros, Thermal physics of asteroids. IV. Thermal infrared beaming. *Astron. Astrophys.* **332**, 1123–1132 (1998).
43. P. Helfenstein, M. K. Shepard, Submillimeter-scale topography of the lunar regolith. *Icarus* **141**, 107–131 (1999).
44. Y. G. Shkuratov, M. A. Kreslavsky, A. A. Ovcharenko, D. G. Stankevich, E. S. Zubko, C. Pieters, G. Arnold, Opposition effect from Clementine data and mechanisms of backscatter. *Icarus* **141**, 132–155 (1999).
45. J. Warell, Properties of the Hermean regolith: IV. Photometric parameters of Mercury and the Moon contrasted with Hapke modelling. *Icarus* **167**, 271–286 (2004).
46. C. M. Pieters, The Moon as a spectral calibration standard enabled by lunar samples: The Clementine example. *New Views Moon* **II**, abstract no. 8025 (1999).
47. P. J. Isaacson, N. E. Petro, C. M. Pieters, S. Besse, J. W. Boardman, R. N. Clark, R. O. Green, S. Lundeen, E. Malaret, S. McLaughlin, J. M. Sunshine, L. A. Taylor, Development, importance, and effect of a ground truth correction for the Moon Mineralogy Mapper reflectance data set. *J. Geophys. Res.* **118**, 369–381 (2013).

48. S. Lundeen, S. McLaughlin, R. Alanis, Moon Mineralogy Mapper Data Product Software Interface Specification, PDS document version 9.10, JPL D-39032 (Jet Propulsion Laboratory, 2011).
49. A. Grumpe, F. Belkhir, C. Wöhler, Construction of lunar DEMs based on reflectance modelling. *Adv. Space Res.* **53**, 1735–1767 (2014).
50. A. Grumpe, C. Wöhler, Recovery of elevation from estimated gradient fields constrained by digital elevation maps of lower lateral resolution. *ISPRS J. Photogramm. Remote Sens.* **94**, 37–54 (2014).
51. E. J. Speyerer, M. S. Robinson, B. W. Denevi; LROC Science Team, Lunar Reconnaissance Orbiter Camera global morphological map of the Moon. *Proc. Lunar Planet. Sci.* **XXXXII**, abstract no. 2387 (2011).

Acknowledgments

Funding: A.A.B. and V.V.S. were supported by the Russian Foundation for Basic Research–Deutsche Forschungsgemeinschaft (RFBR-DFG) grant no. 15-52-12369. C.W. and A.G. were supported by RFBR-DFG grant no. WO 1800/7-1. **Author contributions:** C.W. wrote the major part of the text and prepared the figures. A.G. contributed to the text and generated data for the figures. A.A.B. contributed to the text, analysis of the global OHIBD maps, and discussion of the source and sink mechanisms. V.V.S. contributed to the discussion of the global OHIBD maps and the source and sink mechanisms. **Competing interests:** The authors declare that they have no competing interests. **Data and materials availability:** The global OHIBD maps shown in this paper can be downloaded from the institutional website of the Image Analysis Group at the Technical University of Dortmund University (www.bv.e-technik.tu-dortmund.de/cms/de/forschung/Bildsequenzen_und_Referenzdaten/index.html). All data needed to evaluate the conclusions in the paper are present in the paper and/or the Supplementary Materials. Additional data related to this paper may be requested from the authors.

Submitted 21 April 2017
Accepted 10 August 2017
Published 8 September 2017
10.1126/sciadv.1701286

Citation: C. Wöhler, A. Grumpe, A. A. Berezhnoy, V. V. Shevchenko, Time-of-day–dependent global distribution of lunar surficial water/hydroxyl. *Sci. Adv.* **3**, e1701286 (2017).